

# LONGITUDINAL ELECTRON BUNCH SHAPING EXPERIMENTS AT THE PAL-ITF \*

Seong-Yeol Kim, Ji-Min Seok, Kook-Jine Moon, Moses Chung<sup>†</sup>, UNIST, Ulsan, 689-798, Korea  
 Heung-Sik Kang, Chul Hoon Kim, Juho Hong, Jang-Hui Han, PAL, Pohang, 790-834, Korea  
 J. Thangaraj, Fermilab, Batavia, IL 60510, USA

## Abstract

Longitudinal shaping of electron beam has received much attention recently, due to its potential applications to THz generation, dielectric wakefield acceleration, improvement of FEL performance, and controlled space-charge modulation. Using a set of alpha-BBO crystals, shaping of laser pulse and electron bunch on the order of ps is tested at the Injector Test Facility (ITF) of Pohang Accelerator Laboratory (PAL). Initial experimental results will be presented with analytical theory and numerical simulations

## INTRODUCTION

Bunch- and current-shaping of low energy electron beams are essential beam manipulation techniques for compact light sources, narrowband radiation generation, two-color FEL's, seeding techniques, advanced accelerators, mitigation of collective effects, and diagnostics [1]. To have a precise control of the longitudinal profile of the electron beam, a method to shape the photocathode drive laser is often used.

Several techniques to shape the longitudinal laser pulses of picosecond durations were introduced in recent years, such as line-delay technique, echelon lenses, acousto-optic programmable dispersive filter, or DAZZLER, to mention a few examples. In particular, the direct UV pulse shaping using alpha-BBO crystals is known to be a relatively cheap, compact, and power-efficient technique [2, 3].

In this work, we present initial experimental results on the shaping of laser pulses and electron bunches on the order of ps obtained at the Injector Test Facility (ITF) of Pohang Accelerator Laboratory (PAL) using a set of alpha-BBO crystals. We note that, for the PAL-XFEL, a flat-top longitudinal profile is considered in addition to the nominal Gaussian profile, for the improvement of projected emittances [4]. Using three sets of alpha-BBO crystals, for example, we indeed expect to have a flat-top beam distribution to a good approximation.

## BASIC THEORY

The temporal separation between two polarizations, i.e., the ordinary wave (perpendicular to the optical axis) and the extraordinary wave (parallel to the optical axis) is given by [2]

$$\Delta t = L \left| \frac{1}{v_{ge}} - \frac{1}{v_{go}} \right| = \frac{L}{c} |n_{ge} - n_{go}| = \frac{L}{c} \Delta n_g, \quad (1)$$

\* This work was supported by the 2015 Research Fund (1.150124.01) of UNIST(Ulsan National Institute of Science and Technology)

<sup>†</sup> mchung@unist.ac.kr

where  $L$  is the length of the crystal,  $v_{go} = c/n_{go}$  and  $v_{ge} = c/n_{ge}$  are the group velocities of the o-wave and e-wave respectively. Here,  $c$  is the speed of light in vacuum, and  $n_{go}$  and  $n_{ge}$  are group indices of refraction of the o-wave and e-wave respectively.

We use commercially available alpha-BBO's for this experiment. The high temperature phase Barium Borate (alpha-BBO,  $\alpha$ -BBO) is a negative uniaxial crystal with a strong birefringence (large  $\Delta n_g$ ) over the broad transparent range from 189 nm to 3500 nm. Two alpha-BBO crystals of lengths 7.5 mm and 15 mm are used. Since the spot size of the UV laser (253 nm) used for this experiment is rather big, the clear aperture (diameter) of the alpha-BBO crystals are chosen to be 15 mm. An anti-reflection coating is applied on the surfaces of the alpha-BBO crystals, which also protects the surfaces from ambient moisture. The alpha-BBO crystals are kept inside the clean room to avoid moisture absorption, and they are mounted on the precision rotation stages.

The indices of refraction are given by the Sellmeier equations ( $\lambda$  in  $\mu\text{m}$ ) as (see also Fig. 1)

$$n_o^2 = 2.7471 + 0.01878/(\lambda^2 - 0.01822) - 0.01354\lambda^2, \quad (2)$$

$$n_e^2 = 2.37153 + 0.01224/(\lambda^2 - 0.01667) - 0.01516\lambda^2. \quad (3)$$

The group index of refraction ( $n_g$ ) is calculated from the index of refraction ( $n$ ) as (see also Fig. 2)

$$n_g(\lambda) = n(\lambda) - \left( \frac{dn(\lambda)}{d\lambda} \right) \lambda. \quad (4)$$

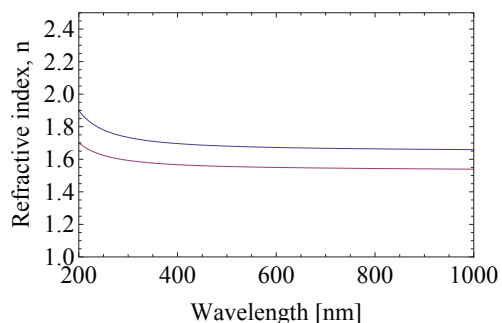


Figure 1: Indices of refraction for o-wave (blue) and e-wave (red) calculated by Sellmeier's formula.

For  $L = 7.5$  mm, we expect  $\Delta t = 6.55$  ps, and for  $L = 15$  mm,  $\Delta t = 13.1$  ps. The laser intensity of multiple Gaussian beams can be approximate as

$$I(t) = \sum_{i=1}^n \frac{1}{n} \exp\left(-\frac{(t-t_i)^2}{2\sigma_i^2}\right). \quad (5)$$

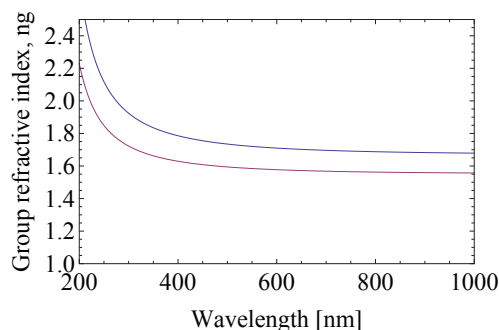


Figure 2: Group indices of refraction for o-wave (blue) and e-wave (red) calculated by Eq. (4).

where  $\sigma_t$  is the rms pulse length of the laser beam. We assumed that the peak intensity of the initial single Gaussian beam is normalized to be 1. Examples of multiply stacked Gaussian beams with  $\text{FWHM} = 2\sigma_t \sqrt{2 \ln 2} = 3$  ps are illustrated in Fig. 3.

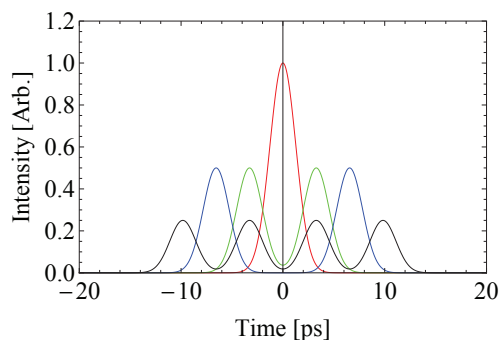


Figure 3: Examples of longitudinal profiles of the multiple Gaussian laser pulses. Each Gaussian has a FWHM of 3 ps. Red curve: single Gaussian, green curve: inserting alpha-BBO crystal of  $L = 7.5$  mm, blue curve: inserting alpha-BBO crystal of  $L = 15$  mm, black curve: inserting both the alpha-BBO crystals.

## INJECTOR TEST FACILITY

To demonstrate performances of the sub-systems of the PAL-XFEL, and to develop high-brightness photo-cathode RF gun and various diagnostic techniques, the injector test facility (ITF) was constructed at PAL [4]. The ITF consists of a photo-cathode RF gun, a 30-mJ Ti:Sa laser system, two S-band (2.856 GHz) accelerating structures, two sets of klystron-modulator systems, and various instrumentations (screens, spectrometer magnets, Turbo Integrated Current Transformer etc.) [5]. A transverse deflecting cavity (S-band, 10-fs resolution) is installed at the end of the beamline, which allows longitudinal beam profile measurements [6]. In this experiment, beam profiles are measured using two YAG scintillator screen (indicated by screen 3 and screen 4 in Fig. 4) imaged with CCD cameras. The typical parameters for the ITF and electron beams are summarized in Table 1.

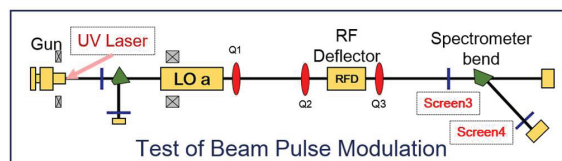


Figure 4: Beam elements and diagnostics setup at the Injector Test Facility (ITF).

Table 1: Summary of the ITF System and Typical Beam Parameters Used for this Experiment

Component	Parameter	Value	Unit
RF-gun	Operating frequency	2.856	GHz
	RF-pulse width	2	$\mu\text{s}$
	Repetition rate	10	Hz
Laser (UV)	FWHM	1.5 ~ 5.5	ps
	Wavelength	253	nm
Deflecting cavity	Operating frequency	2.856	GHz
	Structure length	1061.4	mm
	Operating mode	TM <sub>110</sub>	-
	Temporal resolution	~ 10	fs
	Kick/ $\sqrt{\text{Power}}$	2.7	MV/ $\sqrt{\text{MW}}$
Electron beam	Energy	~ 81	MeV
	Charge	~ 200	pC
	Energy spread (rms)	0.1	%

## LASER SYSTEM

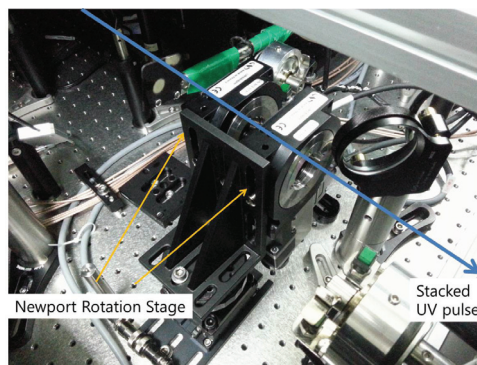


Figure 5: Optics setup for UV laser pulse stacking. The alpha-BBO crystals are mounted on the high-precision rotation stages. Minimum incremental motion of the stages is  $0.0005^\circ$ .

The ITF laser system provides both UV laser beam for the photocathode e-beam gun (see Fig. 5 for the setup used in this experiment) and IR laser beam for the laser heater. The main Ti:sapphire laser system generates >20 mJ picosecond pulses at 760 nm. The spectral bandwidth is limited to 1.5 nm, which is a compromise between good spatial mode in UV conversion and fast rise time in time domain. Time-domain measurement of ps laser pulses is based on the optical cross correlation method using nonlinear mixing in BBO crystal.

To obtain higher time resolution, fs pulses from the oscillator is mixed with the unknown ps pulses. A high speed data acquisition board is used to remove background noise and to measure each pulse of the cross correlation signal [4]. Measurement results with laser pulses of 3 ps FWHM are given in Fig. 6. The  $45^\circ$  orientation angle with respect to the optical axis of the crystal creates equal intensities for e-wave and o-wave [2, 3]. The relative intensity between the two waves could be controlled by a simple rotation of the optics axis. This ramped pulse generation would be investigated in the next experiment run.

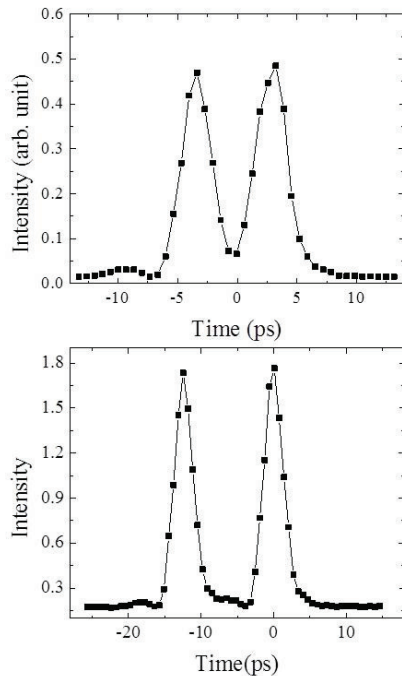


Figure 6: Results of the time-domain measurement of the multi-peak laser pulses:  $L = 7.5$  mm (top) and  $L = 15$  mm (bottom). Time differences between two peaks are measured to be 6.273 ps and 12.3665 ps, respectively, which are slightly smaller than the theoretical estimations.

## RESULTS

To convert the pixel numbers in the screen images into the time difference, we first performed the calibration of the RF deflecting cavity. We measured the pixel numbers of the center of the beam images in screens 3 and 4 by scanning RF phase (1 degree step) of the deflecting cavity. For the operating frequency of 2.856 GHz, we note 1 degrees correspond to 0.973 ps. Based on the calibration data presented in Figs. 7 and 8, we obtain the calibration factors of 7.0735 fs/pixel for screen 3, and 9.5447 fs/pixel for screen 4.

Figure 9 shows the reference beam images generated by the 3 ps FWHM laser pulse. For both images, the measured FWHM's of the electron beam profiles are enlarged. In Figs. 10 and 11, screen images are taken after inserting alpha-BBO crystals of  $L = 7.5$  mm and of  $L = 15$  mm,

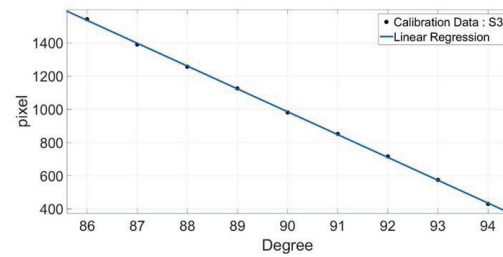


Figure 7: Calibration data for the longitudinal beam profile measurement using deflecting cavity and screen 3.

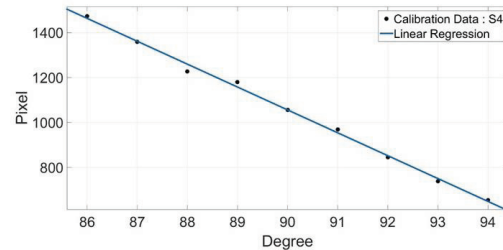


Figure 8: Calibration data for the longitudinal beam profile measurement using deflecting cavity and screen 4.

respectively. For both cases, the time differences between two peaks measured based on screen 3 (4.32 ps and 6.32 ps) are shorter than the analytical estimations (6.55 ps and 13.1 ps) and time-domain measurement of the laser pulses (6.273 ps and 12.3665 ps). Also the general trends are that the profiles estimated from the screen 4 are more widely spread. Particularly for the experiment with the longer crystal ( $L = 15$  mm), the total bunch length increases too much that the transverse focusing is applied unevenly between head and tail (see blurred spots in the upper-left image in Fig. 11). We note that if the transverse beam size is too big, than the projected image generated by the deflecting cavity loses its resolution.

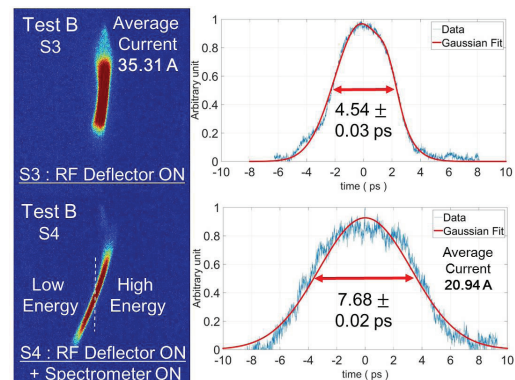


Figure 9: Beam images measured on screen 3 (top row) and screen 4 (bottom row) without inserting BBO crystals. The intensity profiles projected onto the vertical axis indicate time structure of the beam. A 3 ps FWHM laser pulse is used.

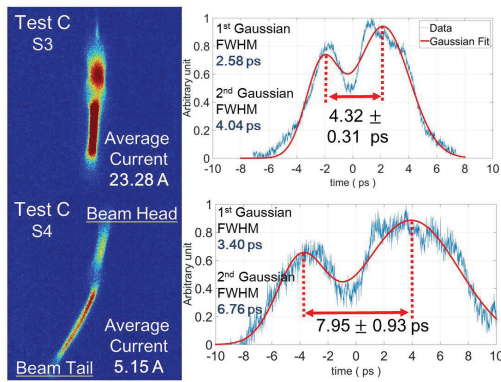


Figure 10: Beam images measured on screen 3 (top row) and screen 4 (bottom row) after inserting BBO crystal of  $L = 7.5$  mm. A 3 ps FWHM laser pulse is used.

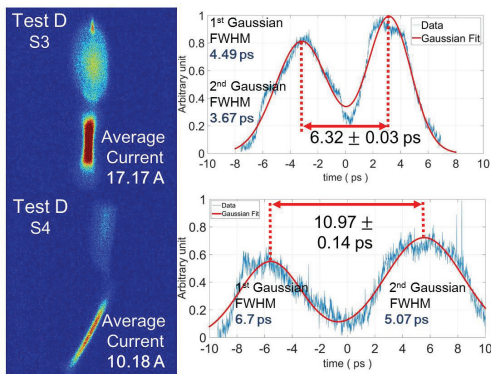


Figure 11: Beam images measured on screen 3 (top row) and screen 4 (bottom row) after inserting BBO crystal of  $L = 15$  mm. A 3 ps FWHM laser pulse is used.

To test the possibility of flat beam profile generation, we apply 5 ps FWHM laser pulse after inserting alpha-BBO crystals of  $L = 7.5$  mm. As illustrated in Fig. 12, it is clear that the two peaks are nearly overlapped and the beam center shows rather flat profile.

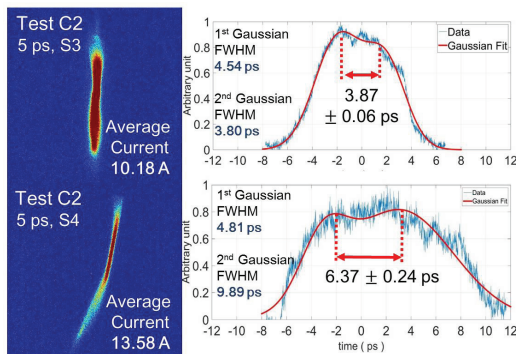


Figure 12: Beam images measured on screen 3 (top row) and screen 4 (bottom row) after inserting BBO crystal of  $L = 7.5$  mm. A 5 ps FWHM laser pulse is used.

To examine the experimental results, we performed numerical simulations using ASTRA and ELEGANT codes.

Since space-charge effects are strong at low beam energies, we used ASTRA code from the photocathode surface to the end of the accelerating cavity (LOa in Fig. 4). For the rest of the beamline, the ELEGANT code has been used to track particles. Reasonable agreements have been obtained as shown in Fig. 13. We plan to run more detailed simulations to fully understand our experimental results.

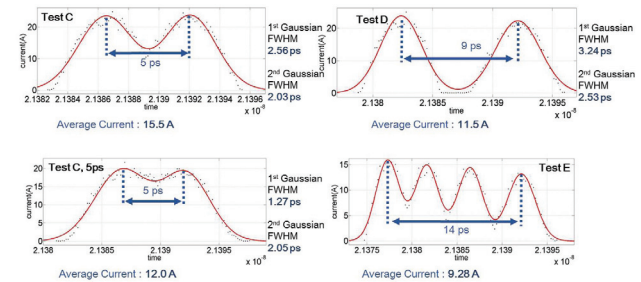


Figure 13: Simulation results obtained from ASTRA and ELEGANT codes.

## CONCLUSIONS AND FUTURE WORK

As future work, we will further investigate methods to generate flat-top beam distributions for the PAL-XFEL. In addition, we plan to study the response of the longitudinally-modulated beam to a dechirper [7]. Understanding the interactions between electron beams of various longitudinal shapes with the wakefields generated by the dechirper will be important to assess the feasibility of the dechirper for use as a deflector.

## REFERENCES

- [1] P. Piot et al., “Overview of Alternative Bunch and Current-Shaping Techniques for Low-Energy Electron Beams”, MOD02, *These proceedings, FEL2015, Daejeon, Korea* (2015).
- [2] J.G. Power et al., “High Frequency Bunch Train Generation from an RF Photoinjector at the AWA”, MO6RFP047, *Proceedings of PAC09, PAC’09, Vancouver, BC, Canada* (2009).
- [3] J. Thangaraj et al., “Z-SHAPER: A Picosecond UV Laser Pulse Shaping Channel at the Advanced Superconducting Test Accelerator”, THPP059, *Proceedings of LINAC2014, LINAC’14, Geneva, Switzerland* (2014).
- [4] *PAL-XFEL Technical Design Report* (Pohang Accelerator Laboratory, 2013).
- [5] J. Hong et al., “Beam Measurement of Photocathode RF-Gun for PAL-XFEL”, THP011, *Proceedings of FEL2014, FEL’14, Basel, Switzerland* (2014).
- [6] J.-H. Lee et al., “Slice Emittance Measurement Using RF Deflecting Cavity at PAL-XFEL ITF”, TUP013, *Proceedings of FEL2014, FEL’14, Basel, Switzerland* (2014).
- [7] H.-S. Kang et al., “A Beam Test of Corrugated Structure for Passive Linearizer”, TUP093, *Proceedings of FEL2014, FEL’14, Basel, Switzerland* (2014).